Solving integral equations in free space with inverse-designed ultrathin optical metagratings

🔴 Check for updates

Andrea Cordaro ●[1,2] ✉, Brian Edwards[3], Vahid Nikkhah[3], Andrea Alù ●[4,5], Nader Engheta[3] & Albert Polman[2]

As standard microelectronic technology approaches fundamental limitations in speed and power consumption, novel computing strategies are strongly needed. Analogue optical computing enables the processing of large amounts of data at a negligible energy cost and high speeds. Based on these principles, ultrathin optical metasurfaces have been recently explored to process large images in real time, in particular for edge detection. By incorporating feedback, it has also recently been shown that metamaterials can be tailored to solve complex mathematical problems in the analogue domain, although these efforts have so far been limited to guided-wave systems and bulky set-ups. Here, we present an ultrathin Si metasurface-based platform for analogue computing that is able to solve Fredholm integral equations of the second kind using free-space visible radiation. A Si-based metagrating was inverse-designed to implement the scattering matrix synthesizing a prescribed kernel corresponding to the mathematical problem of interest. Next, a semitransparent mirror was incorporated into the sample to provide adequate feedback and thus perform the required Neumann series, solving the corresponding equation in the analogue domain at the speed of light. Visible wavelength operation enables a highly compact, ultrathin device that can be interrogated from free space, implying high processing speeds and the possibility of on-chip integration.

The world's ever-growing need for efficient computing has been driving researchers from diverse research fields to explore alternatives to the current digital computing paradigm. The processing speed and energy efficiency of standard electronics have become limiting factors for novel disruptive applications entering our everyday life, such as artificial intelligence, machine learning, computer vision and many more. In this context, analogue computing has resurfaced and regained substantial attention as a complementary route to traditional architectures[1–4]. Specifically, the tremendous recent advances in the field of metamaterials and metasurfaces have been unlocking new opportunities for all-optical computing strategies, given the possibility of shaping optical fields in extreme ways over subwavelength thicknesses. The absence of bulky optical elements, in turn, enables on-chip integration, paving the way for hybrid optical and electronic data processing.

[1]Institute of Physics, University of Amsterdam, Amsterdam, The Netherlands. [2]Center for Nanophotonics, Institute AMOLF, NWO, Amsterdam, The Netherlands. [3]Department of Electrical and Systems Engineering, University of Pennsylvania, Philadelphia, PA, USA. [4]Photonics Initiative, Advanced Science Research Center, City University of New York, New York, NY, USA. [5]Physics Program, Graduate Center, City University of New York, New York, NY, USA. ✉e-mail: a.cordaro@amolf.nl;
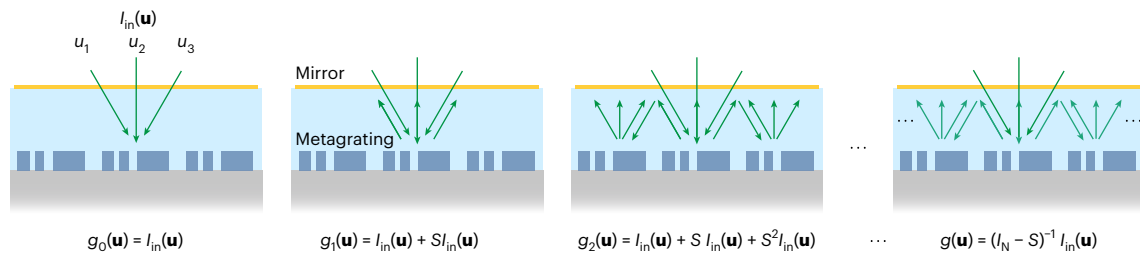
Fig. 1 | Si metagrating-based integral equation solver. An input vector $\mathbf{I}_{in}$ is fed to the system in the form of N plane waves with different complex amplitudes incident along N diffraction channels. The signal interacts repeatedly with a metagrating, bouncing back from a partially reflecting mirror, each time multiplied by the metagrating scattering matrix and therefore building up the terms of a Neumann series of subsequent matrix multiplications required to solve the integral equation. For the sake of simplicity, the formulas underneath the panels do not take into account the semitransparent mirror scattering matrix at this stage.

The idea of using light to outsource specific computing tasks comes with several advantages. First, there is a clear enhancement in processing speeds as the computation is performed at the speed of light travelling through metamaterials with typical sizes smaller than or comparable with the wavelength of operation. Also, processing signals in the optical domain enable massive parallelization and may potentially avoid unnecessary analogue-to-digital conversion. As an example, recent works have shown how several image processing tasks can be performed before the image is discretized into pixels[5–19], relying on the possibility of engineering the angular response of metasurfaces and hence imparting instantaneously a mathematical operation to the spatial content of an input signal[11,12,20]. Finally, analogue computing meta-devices can be passive, implying an extremely low energy usage. Recently, broader applications of this approach have been appearing in different fields, ranging from silicon photonics[21–23] to organic neuro-morphic electronics[24,25], that is, architectures that mimic the biological brain's function, and even acoustics[26–28].

A key question is whether it is possible to go beyond simple image processing tasks and focus on a more complex mathematical problem, such as solving an integro-differential equation. The concept of a wave-based integral equation solver has been recently demonstrated in the microwave regime for symmetric and non-symmetric kernels and in a multi-frequency parallel fashion[29,30], but relying on guided waves in bulky metamaterial set-ups. An important next challenge is to demonstrate if such a complex mathematical operation can be carried out in the optical spectral range, ideally within an ultrathin form factor that can be interrogated through free-space radiation and easily combined with similar devices to represent operator composition. This will enable the fabrication of far more compact on-chip devices operated at wavelengths that are widely used for communication technology. This dramatic size reduction further implies a drastic increase in processing speeds, as light has to travel much shorter distances.

Here, we demonstrate a Si metasurface-based optical platform that combines a tailored scattering matrix design and a feedback system to enable the solution of Fredholm integral equations of the second kind from the far field:

$$g(u) = I_{in}(u) + \int_a^b K(u,v)\,g(v)\,\mathrm{d}v, \qquad (1)$$

where $g(u)$ is the unknown solution of equation (1), $K(u,v)$ is the kernel of the integral operator and $I_{in}(u)$ is an arbitrary input function. Mathematically, this form of equation may be analytically solvable if it is in separable form or for some special kernels, and an inversion formula may exist (for example, a Fourier transform). However, when certain convergence conditions for the kernels are satisfied[29,31,32], a general technique to solve equation (1) is to exploit the Neumann successive approximation method: we assume an initial guess $g_0(u) = I_{in}(u)$, and successive approximations can be obtained by evaluating $g_{i+1}(u) = I_{in}(u) + \int_a^b K(u,v)\,g_i(v)\,\mathrm{d}v$, whereupon eventually $g_n(u)$ converges to the solution $g(u)$ as $n \to \infty$ (ref. 31). Here, we show how to physically implement this iterative procedure in an analogue fashion employing a Si metasurface coupled to a feedback system.

First, equation (1) is discretized by sampling its independent variables, u and v, over N points in the interval (a, b) to form two vectors with such variables, $\mathbf{u}$ and $\mathbf{v}$. The application of the integral operator $\int_a^b K(u,v)[\ ]\,\mathrm{d}v$ on the function $g(u)$ is then analogous to the multiplication (or application) of a matrix operator $K = K(\mathbf{u}, \mathbf{v})\frac{(a-b)}{N}$ on a vector $\mathbf{g} = g(\mathbf{u})$. Thus, equation (1) may be numerically approximated by the $N \times N$ matrix equation

$$\mathbf{g} = \mathbf{I}_{in} + K\mathbf{g} \qquad (2)$$

Second, the solution $\mathbf{g}$ is represented as a Neumann series $\mathbf{g} = \sum_n (\mathrm{K})^n \mathbf{I}_{in} = (I_N - K)^{-1}\mathbf{I}_{in}$, where I_N is the $N \times N$ identity matrix. The convergence of the Neumann series demonstrates that the inverse operator $(I_N - K)^{-1}$ exists.

Next, it is possible to think of the N mathematical sampling points as N discrete physical modes, and thus $\mathbf{g}$ is a vector representing the complex amplitude of these modes on a given plane with a chosen direction. The integral operator can then be represented by a scattering matrix that performs matrix multiplication between these sets of modes.

If we consider a periodic metagrating, the input/output modes can be mapped into the N discrete diffraction channels determined by the periodicity and the wavelength, while the discretized integral operator K can be mapped onto the metasurface scattering matrix S that governs the coupling between these channels. Following the schematics in Fig. 1, the discretized input $\mathbf{I}_{in}$ is a vector of length N containing the complex amplitudes of the plane waves addressing the system via its available diffraction channels, acting as seed guess $\mathbf{g}_0 = \mathbf{I}_{in}$. The vector is multiplied by the metasurface scattering matrix upon its first reflection, resulting in a more refined guess $\mathbf{g}_1$ to the solution of the integral equation associated with K. The signal is then reflected by a semitransparent mirror and fed back to the grating for the next iteration. Intuitively, the system performs an analogue Neumann series at the speed of light by iteratively applying the S matrix on the seed vector through multiple reflections, in the same way the mathematical integral operator is applied repeatedly on the initial guess function.

The entire computing metastructure is therefore composed of two elements: (1) a metagrating with a period that determines the number of input/output modes (grating orders) and a unit cell with tailored geometry defining the scattering matrix of interest and (2) a semitransparent mirror enabling feedback and in-coupling combined with a spacer layer.
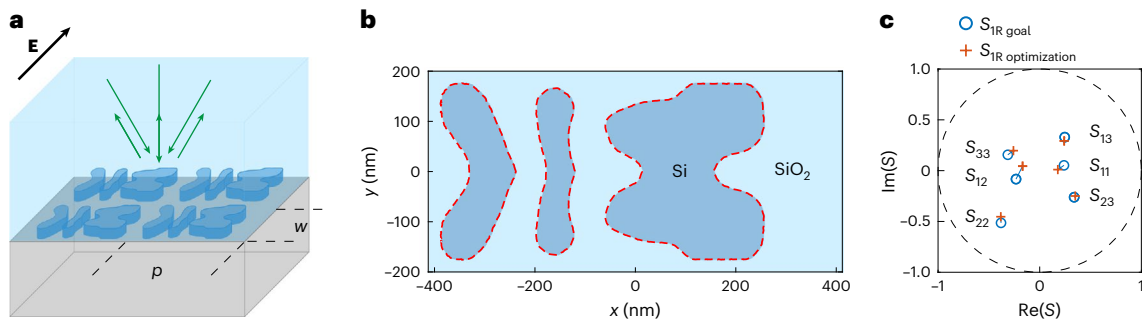
Fig. 2 | Kernel design. a, Schematic illustration of a two-dimensional metagrating (periodicities p and w) with a suitably engineered unit cell geometry. The black arrow indicates the polarization (Transverse Electric, TE) of the incoming **E** field. **b**, Top view of the optimum metagrating unit cell made of Si (blue) and SiO$_2$ (light blue). **c**, Simulation results for the S_{1R} matrix elements of the inverse-designed metagrating (red crosses) and the corresponding desired matrix elements (blue circles).

Kernel design

The key requirement is the careful design of the metagrating unit cell to synthesize the prescribed S matrix

$$S_1 = \begin{pmatrix} S_{1R} & S_{1T}{}^\top \\ S_{1T} & S_{1R'} \end{pmatrix} \tag{3}$$

where S_{1R} and S_{1T} are the reflection and transmission sub-blocks, while $S_{1R'}$ represents reflection from the substrate side. Since the Neumann series is performed in reflection, only the reflection sub-block S_{1R} needs to be designed: it contains the complex reflection coefficients connecting the diffraction channels in the spacer layer above the metagrating. To prove the generality of our approach, we began our problem by choosing a random passive and reciprocal (that is, symmetric) matrix with $N = 3$:

$$S_{1R} = \begin{pmatrix} 0.239 + 0.052\,i & -0.233 - 0.083\,i & 0.246 + 0.329\,i \\ -0.233 - 0.083\,i & -0.381 - 0.514\,i & 0.339 - 0.262\,i \\ 0.246 + 0.329\,i & 0.339 - 0.262\,i & -0.314 + 0.156\,i \end{pmatrix}. \tag{4}$$

Next, we set the periodicities p and w of the grating (Fig. 2a) to have three diffraction orders in reflection at the target wavelength $\lambda_0 = 706$ nm. We choose this wavelength because (1) Si is rather transparent, (2) light sources in this spectral range are readily accessible and (3) the corresponding submicrometre unit cell footprint enables compact circuit design and integration. Specifically, we choose $p = 825$ nm while the orthogonal periodicity $w = 400$ nm is set to be subwavelength. This enhances the degrees of freedom for the unit cell design without opening additional diffraction channels. We optimize the metagrating unit cell geometry using the adjoint method[33–37], setting the height h of the etched silicon nanostructure to 150 nm. The resulting optimized unit cell (Fig. 2b) consists of a Si nanostructure on a sapphire substrate embedded in a transparent SiO$_2$ spacer layer[38–40]. The figure of merit (FOM) to be minimized during the optimization is the sum of the squared 'distances' on the complex plane between the complex-valued matrix elements of the S matrix of a designed geometry (as in Fig. 2b) and the prescribed ones in equation (4): FOM $= \sum_{i,j} \left| S_{1R_{ij}} - S_{1R\,\text{optimization}_{ij}} \right|^2$ (Supplementary Information).

As shown in Fig. 2c, the optimized metagrating approximates very well the desired S matrix, achieving a figure of merit as low as 0.058. This demonstrates that it is possible to inverse-design metagratings with a prescribed S matrix, showing the feasibility of this optical computing concept for the solution of integral equations with a wide range of kernels. As shown in the literature[41], a similar inverse-designed metagrating can be quickly generated by neural networks after adequate training on images of topology-optimized unit cells. We envision a similar strategy for our proposed scheme, hence making it possible to rapidly converge to a metagrating design given a certain kernel matrix.

Compared to optical vector–matrix multiplication systems put forward in the literature[42–46] that consist of bulky optical elements, the metagrating proposed here realizes matrix multiplication in phase and amplitude in a single subwavelength-thick surface. This is a massive advantage as it opens up the possibility of hybrid analogue–digital platforms on a single chip, where the analogue part can ease the burden of standard digital computing. Moreover, a thin platform is less prone to phase errors due to long propagation distances.

Analogue matrix inversion

What we have discussed so far concerns only the design of the metagrating scattering matrix mapping the discretized integral kernel operator K in equation (2). Next, to find the solution of the integral equation, it is crucial to have a feedback system that repeatedly returns the signal reflected from the metagrating back to it so that the Neumann series is constructed. To this end, the SiO$_2$ spacer is covered with a 15-nm-thick Au layer to form a semitransparent mirror (Fig. 3a)[47]. The distance between the metagrating and mirror is 487 nm $\approx \lambda_0/n$SiO$_2$ (where nSiO$_2$ is the SiO$_2$ refractive index) to avoid near-field coupling, which may introduce additional modes into the system. The S matrix characterizing the mirror is

$$M = \begin{pmatrix} M_R & M_T{}^\top \\ M_T & M_{R'} \end{pmatrix} \tag{5}$$

where M_R and $M_{R'}$ are the sub-blocks representing reflection from the air and SiO$_2$ side respectively, and M_T is the transmission counterpart. Including the mirror, the scattering matrix of the entire metastructure (grating, SiO$_2$ spacer and mirror) becomes

$$S_2 = \begin{pmatrix} S_{2R} & S_{2T}{}^\top \\ S_{2T} & S_{2R'} \end{pmatrix} \tag{6}$$

The Neumann series, and thus the solution of equation (2), is embedded in S_2. The transmission of the entire stack, as measured in our experiment, is composed of a sum of terms each corresponding to an increasing number of interactions with the metagrating (Figs. 1 and 3a)[48]:

$$S_{2T} = S_{1T}M_T + S_{1T}M_{R'}S_{1R}M_T + S_{1T}(M_{R'}S_{1R})^2 M_T + \ldots$$
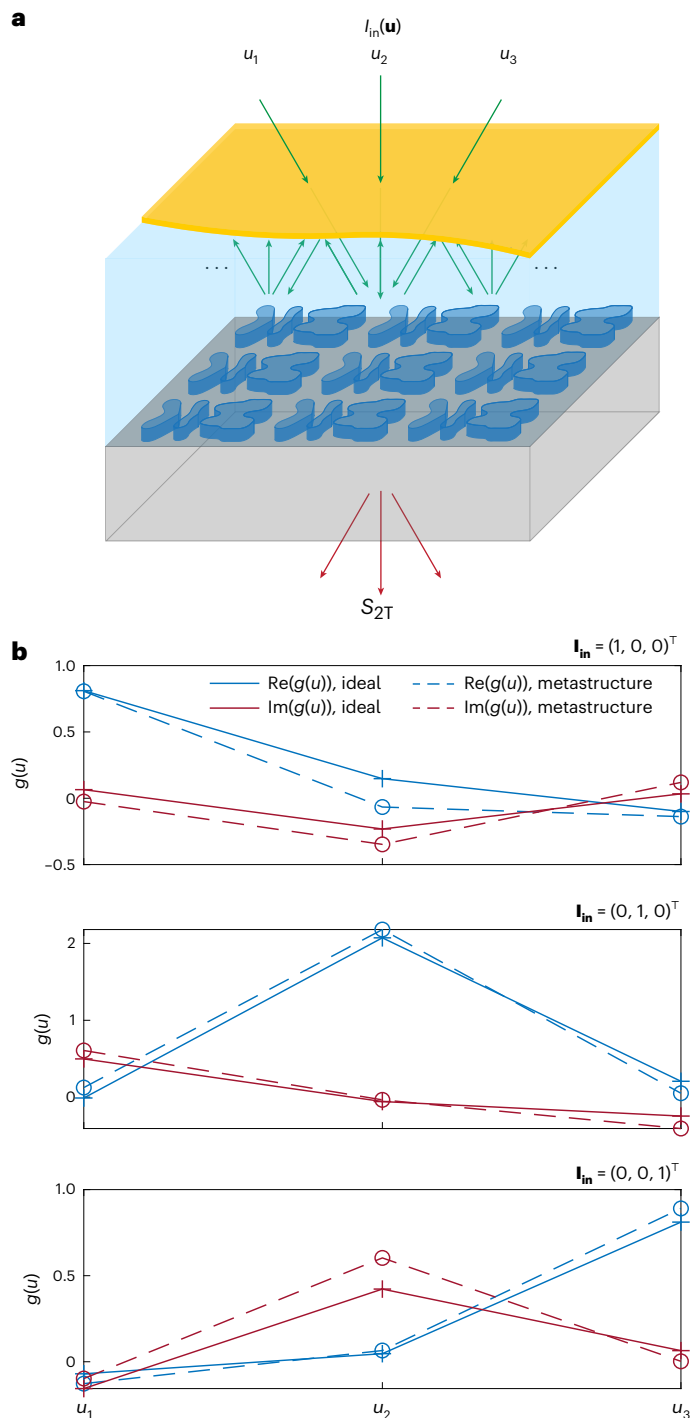$$= S_{1T}(I_3 - M_{R'}S_{1R})^{-1}M_T. \tag{7}$$

Fig. 3 | Analogue matrix inversion. a, The solution of equation (2) is built up inside the spacer layer in the form of a collection of complex wave amplitudes, one for each discrete diffraction channel. The solution is outcoupled and read out in transmission. **b,** Analogue solution (real (Re) and imaginary (Im) parts) of the integral equation (dashed lines) obtained from the simulation results for the metastructure transmission, compared with the ideal theoretical solution $\mathbf{g} = (I_N - K)^{-1}\mathbf{I}_{in}$ (solid lines), for the three orthogonal input vectors $(1, 0, 0)^T$, $(0, 1, 0)^T$ and $(0, 0, 1)^T$. The wavelength of operation in this simulation is $\lambda_0 = 706$ nm.

The transmission sub-block S_{2T} is composed of the inverse operator $(I_3 - M_{R'}S_{1R})^{-1}$ solving equation (2) multiplied by the mirror transmission M_T and by the metasurface transmission S_{1T}. In other words, light is coupled into the system passing through the mirror first, and

then the solution is outcoupled via the metasurface. Hence, to extract the solution computed by the metastructure, that is, the linear combination of complex amplitudes of the diffracted modes inside the spacer layer that converges after multiple passes, M_T and S_{1T} must be de-embedded from S_{2T}. Figure 3b compares the solution $S_{1T}^{-1}S_{2T}M_T^{-1}$ provided by the simulated metastructure transmission to the ideal solution of equation (2) with $K = M_{R'}S_{1R}$ and $\mathbf{I}_{in}$ equal to the vectors belonging to the canonical basis generating the space of all possible input vectors (that is, $(1, 0, 0)^T$, $(0, 1, 0)^T$ and $(0, 0, 1)^T$). Any input vector can be expressed as a linear combination of these, and given the linearity of the metasurface, agreement in the response for these basic excitations ensures that the structure can solve the integral equation problem for arbitrary inputs. The metasurface-based analogue solution and the ideal solution show good agreement for all the inputs, both in terms of the real and imaginary parts. Minor discrepancies are ascribed to the small difference between the desired S matrix and the optimized one (Fig. 2c) and this result demonstrates that it is possible to design the desired kernel K and invert $(I_N - K)$ in a fully analogue fashion.

Nanofabrication and optical characterization

Next, we present the experimental implementation of an all-optical integral-equation-solving metasurface using the optimized geometry described above. The analogue solution of equation (2) is built up inside the spacer layer in the form of a collection of complex wave amplitudes. Despite the fact that the complex amplitudes readily exist just below the surface of the kernel and can be utilized by another similar device as the one presented herein, these values are hard to retrieve in the far field, where a meaningful phase reference at each angle is difficult to define. Hence, similar to spectral reflectometry, we obtain a more robust measurement by comparing the spectroscopic power measurements over a broad wavelength range to simulations of the optimized structure. Within spectral reflectometry, a limited number of chosen parameters such a material layer thickness, Lorentz oscillator frequency, damping coefficients and so on are fitted to a vastly overdetermined system to obtain Kramers–Kronig-safe models from which any value can be derived, including complex amplitudes within a material stack at a specific frequency. Here we do something similar and allow ourselves only one fitted parameter, a dilation operation on the structure, possibly representing fabrication complications, to generate internally consistent spectral traces for all of the possible inputs. We show that minor perturbations of this single parameter are enough to generate an excellent fit and use this data to retrieve an estimate for the experimental solution provided by the metastructure.

First, the optimized metagrating geometry was patterned over a 150-nm-thick Si(100) film on a sapphire (Al_2O_3) substrate by means of electron-beam lithography and reactive ion etching. Next, the metasurface was embedded in SiO_2 by spin coating and annealing a silica glass sol–gel layer that planarizes the structure, followed by a final SiO_2 sputtering that allows fine control of the total spacer thickness. Finally, a 15-nm-thick Au layer was evaporated on the structure using an organic adhesion monolayer (details concerning the fabrication can be found in the Methods)[49,50].

First, we analyse the fabricated Si metasurface without the SiO_2 spacer and the semitransparent mirror. As shown in Fig. 4a, the fabricated structures after the Si reactive ion etching step are uniform and smooth over a large area. Next, it is important to compare the optimized unit cell to the experimental one. Figure 4b shows that the etched unit cell follows very closely the optimized contour (red dashed lines in Figs. 2b and 4b). To corroborate this feature, the transmittance of normal incident light to the zeroth diffraction order was measured and compared to its simulated counterpart. In the simulation, the optimized structure described above was used. The transmittance spectrum was acquired over a broad wavelength range ($\lambda_0 = 500$–800 nm) to obtain maximum sensitivity in the comparison between experiment and simulation. Figure 4c demonstrates strong agreement between simulated and

measured optical spectra, further confirming the suitability of the combined electron-beam lithography and reactive ion etching process to fabricate precisely tailored metagratings for analogue optical computing in the visible spectral range.

Next, the cross-section in Fig. 4d shows how the SiO_2 spacer conformally embeds the metagrating with no detectable air inclusions, creating a smooth planar top surface. The final thickness of the layer with the embedded metagrating amounts to 638 nm. Again, the transmittance is measured at this step, once more experimentally reproducing the key features present in the simulated ideal spectrum (Fig. 4e). The small discrepancies between experiment and simulation in Fig. 4c–e can be attributed to minor fabrication imperfections, such as a slight difference in the SiO_2 refractive index between experiment and simulation, unintended resist overexposure or underexposure and non-perfectly straight Si etching. Finally, the Au film evaporation concludes the fabrication, providing the metastructure with a semitransparent mirror, and hence the required feedback system.

Figure 5 shows the measured transmittance spectra of the fully fabricated metastructure relating to each S parameter belonging to S_{2T} or, equivalently, the fraction of transmitted light going into each diffraction channel when the metastructure is illuminated through each input channel above the mirror. Specifically, each panel shows the amplitudes squared of the elements belonging to each column of S_{2T}. Note that the input and output angles are changing with the wavelength of illumination according to the grating equation (Methods). Each panel in Fig. 5 also shows the simulated spectra of the designed ideal metastructure in Fig. 3a that gives the solutions shown in Fig. 3b.

The agreement over a broad wavelength range between simulation and experiment is clear: for each matrix element, the spectral features present in the simulation are reproduced experimentally. Small discrepancies between experiment and simulation are attributed to minor fabrication imperfections, as described above. Finally, taking advantage of the broad wavelength range of the data and minor perturbations to the structure in the simulation, it is possible to retrieve an estimate for the experimental solution provided by the fabricated metastructure, including its uncertainty (Supplementary Information). Figure 6 compares the latter experimental solution to the ideal solution of equation (2) for the canonical inputs $(1, 0, 0)^\top$, $(0, 1, 0)^\top$ and $(0, 0, 1)^\top$. Although the accuracy of the solution is reduced compared to that shown in Fig. 3b and the wavelength of operation is blueshifted by 7 nm, the good agreement and similar trend with the ideal solution demonstrates the all-optical integral-equation-solving concept experimentally.

Conclusions

We have presented a Si-based optical metastructure that solves Fredholm integral equations of the second kind in a fully analogue fashion at optical frequencies. First, we stated the mathematical problem in terms of the Neumann series (that is, successive approximations). Next, we discussed the analogy between the solving of the integral equation and the behaviour of an optimized periodic metagrating

coupled to a feedback system. At the foundations of this mapping lies the possibility of designing the S matrix of a periodic structure by setting its periodicity (that is, the number of input/output modes and hence the dimension of the S matrix) and optimizing its unit cell (that is, optimizing the coupling of light into the defined diffraction modes
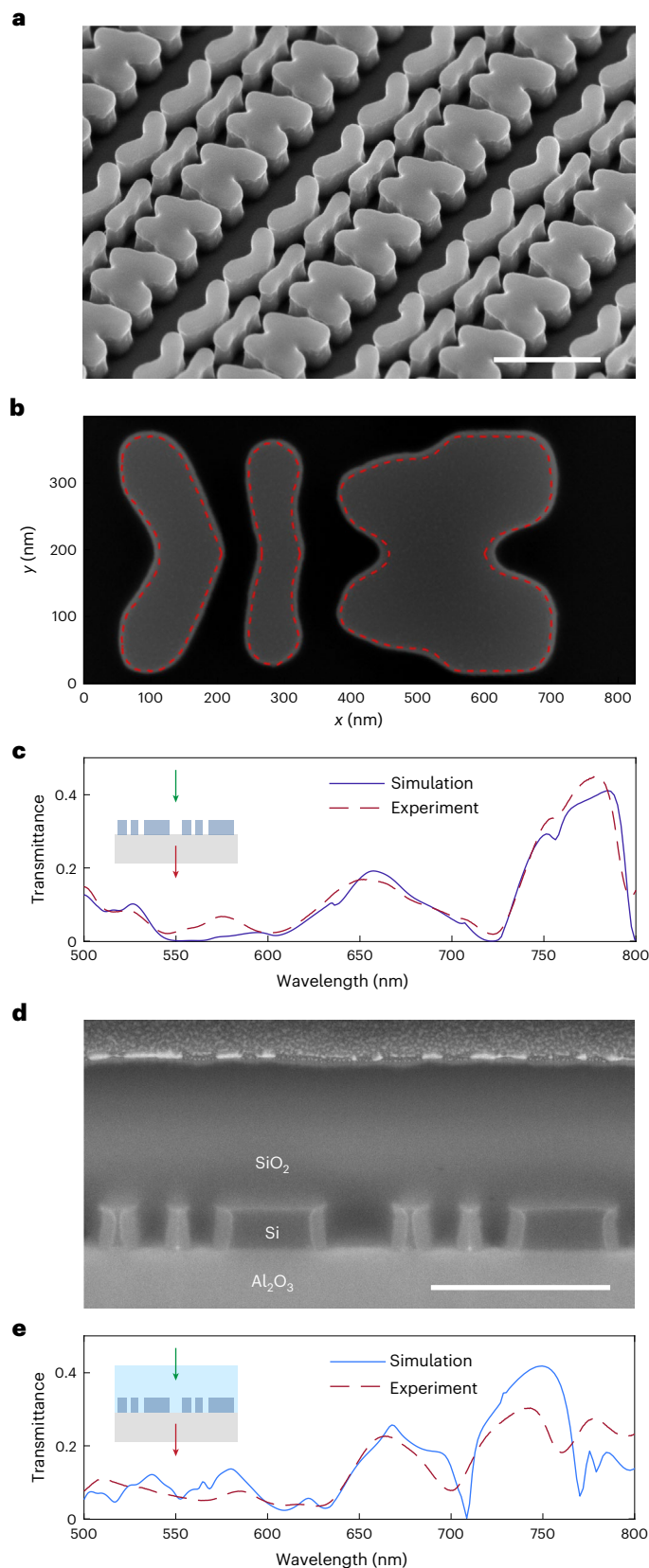
Fig. 4 | Fabrication and optical characterization of the optical analogue integral equation solver. a, Tilted scanning electron microscopy (SEM) image of the patterned Si metagrating. Scale bar, 500 nm. **b**, Zoomed-in top-view SEM image of a single unit cell compared with the desired optimized contour (red dashed line). **c**, Experimental (dashed red line) and simulated (dark blue line) transmittance spectra of the metagrating after the Si etch step (that is, without silica spacer and top mirror). The sample was illuminated under normal incidence (green arrow) and the transmitted zeroth-order diffraction intensity was collected (red arrow, inset) as a function of incident wavelength. **d**, SEM image of a focused-ion-beam-milled cross-section of the same metagrating embedded in a SiO_2 spacer. Scale bar, 500 nm. **e**, Experimental (dashed red line) and simulated (blue line) transmittance spectra of the metagrating after the SiO_2 planarization step. The input polarization is TE for **c** and **e**.
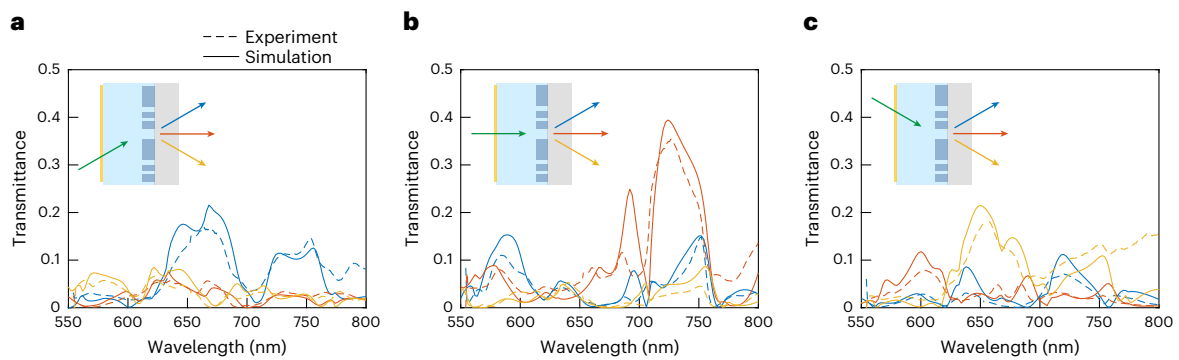
Fig. 5 | Optical characterization of S_{2T}. a–c, Experimental (dashed lines) and simulated (solid lines) transmittance spectra of the completed metastructure. Insets show a schematic visualization of the metastructure indicating the exciting input port (green arrows) representing orthogonal unit vectors, and the three output ports (yellow, orange and blue arrows, matching the corresponding spectra). The input polarization is TE for all panels.
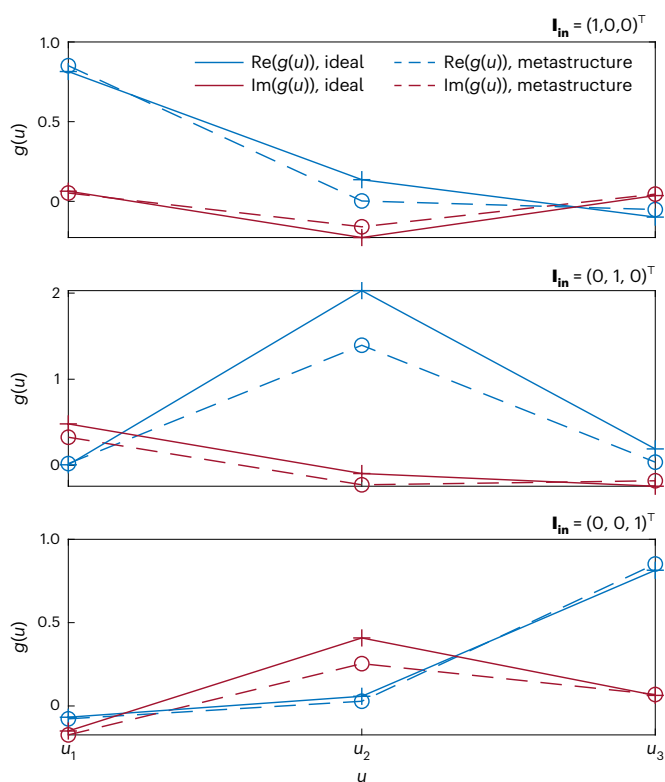
Fig. 6 | Estimated experimental solution. Estimated experimental analogue solution (real and imaginary parts) of the integral equation (dashed lines; Supplementary Information) compared with the ideal theoretical solution (solid lines). The wavelength of operation is $\lambda_0 = 699$ nm.

the standard double-precision, that is 64 bits) in 60 iterations, corresponding to a processing time of about 349 fs, orders of magnitude faster than the clock speed of a conventional processor (Supplementary Fig. 3). Operation in the visible spectral range in combination with deep-subwavelength fabrication resolution creates metastructures that are submicrometres thick. This represents a very high degree of circuit integration given the complexity of the mathematical operation performed in this small volume.

Interestingly, the same metagrating–feedback iterative approach can also be applied to Fredholm integral equations of the first kind. Moreover, it is possible to scale up the dimensionality of the problem, increasing the number of input/output ports by using more diffraction orders or by encoding information in the polarization state of light (Supplementary Information)[35,51]. One key advantage of our scheme is the possibility of integrating many designs within a unique feedback system, thus enabling parallelization whenever this is compatible with the problem under study.

Further extensions of this work may explore non-symmetric kernels in a transmissive set-up and include nonlinear materials within the feedback system (for example, replacing the SiO_2 spacer layer) to explore nonlinear mathematical problems. Additionally, nonlinearity could also be applied after processing the information via linear operations with a dedicated external nonlinear device.

Finally, switchable metagratings (for example, using phase change materials or mechanical modulation) could be envisioned to dynamically tune the encoded mathematical operation, paving the way for all-optical reconfigurable computing circuitry, solving problems of further enhanced complexity.

Online content

Any methods, additional references, Nature Portfolio reporting summaries, source data, extended data, supplementary information, acknowledgements, peer review information; details of author contributions and competing interests; and statements of data and code availability are available at https://doi.org/10.1038/s41565-022-01297-9.

References

1. Athale, R. & Psaltis, D. Optical computing: past and future. *Opt. Photon. News* **27**, 32–39 (2016).
2. Solli, D. R. & Jalali, B. Analog optical computing. *Nat. Photon.* **9**, 704–706 (2015).
3. Zangeneh-Nejad, F., Sounas, D. L., Alù, A. & Fleury, R. Analogue computing with metamaterials. *Nat. Rev. Mater.* **6**, 207–225, (2020).
4. Silva, A. et al. Performing mathematical operations with metamaterials. *Science* **343**, 160–163 (2014).

in amplitude and phase). Consequently, we showed how the designed metastructure effectively solves the problem of interest and compared the metasurface-based solution to the ideal solution. We showed that electron-beam lithography and reactive ion etching provide the spatial resolution required to create a hardware representation of a predefined kernel, with relatively small deviations between experiment and simulations. We optically characterized the output for different input signals, showing good agreement with the ideal simulated response.

Our results demonstrate the possibility of solving complex mathematical problems and a generic matrix inversion at speeds that are far beyond those of typical digital computing methods. The solution converges (within a difference from the infinite sum that is smaller than

5. Zhu, T. et al. Plasmonic computing of spatial differentiation. *Nat. Commun.* **8**, 15391 (2017).

6. Zhu, T. et al. Generalized spatial differentiation from the spin Hall effect of light and its application in image processing of edge detection. *Phys. Rev. Appl.* **11**, 034043 (2019).

7. Zhu, T. et al. Topological optical differentiator. *Nat. Commun.* **12**, 680 (2021).

8. Guo, C., Xiao, M., Minkov, M., Shi, Y. & Fan, S. Photonic crystal slab Laplace operator for image differentiation. *Optica* **5**, 251–256 (2018).

9. Guo, C., Xiao, M., Minkov, M., Fan, S. & Shi, Y. Isotropic wavevector domain image filters by a photonic crystal slab device. *J. Opt. Soc. Am. A* **35**, 1685–1691 (2018).

10. Wang, H., Guo, C., Zhao, Z. & Fan, S. Compact incoherent image differentiation with nanophotonic structures. *ACS Photon.* **7**, 338–343 (2020).

11. Kwon, H., Sounas, D., Cordaro, A., Polman, A. & Alù, A. Nonlocal metasurfaces for optical signal processing. *Phys. Rev. Lett.* **121**, 173004 (2018).

12. Cordaro, A. et al. High-index dielectric metasurfaces performing mathematical operations. *Nano Lett.* **19**, 8418–8423 (2019).

13. Youssefi, A., Zangeneh-Nejad, F., Abdollahramezani, S. & Khavasi, A. Analog computing by Brewster effect. *Opt. Lett.* **41**, 3467–3470 (2016).

14. Momeni, A., Rajabalipanah, H., Abdolali, A. & Achouri, K. Generalized optical signal processing based on multioperator metasurfaces synthesized by susceptibility tensors. *Phys. Rev. Appl.* **11**, 064042 (2019).

15. Abdollahramezani, S., Hemmatyar, O. & Adibi, A. Meta-optics for spatial optical analog computing. *Nanophotonics* **9**, 4075–4095 (2020).

16. Moeini, M. M. & Sounas, D. L. Discrete space optical signal processing. *Optica* **7**, 1325–1331 (2020).

17. Zhou, Y., Zheng, H., Kravchenko, I. I. & Valentine, J. Flat optics for image differentiation. *Nat. Photon.* **14**, 316–323 (2020).

18. Pors, A., Nielsen, M. G. & Bozhevolnyi, S. I. Analog computing using reflective plasmonic metasurfaces. *Nano Lett.* **15**, 791–797 (2015).

19. Bykov, D. A. et al. First-order optical spatial differentiator based on a guided-mode resonant grating. *Opt. Express* **26**, 10997–11006 (2018).

20. Kwon, H., Cordaro, A., Sounas, D., Polman, A. & Alù, A. Dual-polarization analog 2D image processing with nonlocal metasurfaces. *ACS Photon.* **7**, 1799–1805 (2020).

21. Bogaerts, W. et al. Programmable photonic circuits. *Nature* **586**, 207–216 (2020).

22. Shen, Y. et al. Deep learning with coherent nanophotonic circuits. *Nat. Photon.* **11**, 441–446 (2017).

23. Shastri, B. J. et al. Photonics for artificial intelligence and neuromorphic computing. *Nat. Photon.* **15**, 102–114 (2021).

24. van de Burgt, Y. et al. A non-volatile organic electrochemical device as a low-voltage artificial synapse for neuromorphic computing. *Nat. Mater.* **16**, 414–418 (2017).

25. Van De Burgt, Y., Melianas, A., Keene, S. T., Malliaras, G. & Salleo, A. Organic electronics for neuromorphic computing. *Nat. Electron.* **1**, 386–397 (2018).

26. Zangeneh-Nejad, F. & Fleury, R. Performing mathematical operations using high-index acoustic metamaterials. *New J. Phys.* **20**, 073001 (2018).

27. Zangeneh-Nejad, F. & Fleury, R. Topological analog signal processing. *Nat. Commun.* **10**, 2058 (2019).

28. Hughes, T. W., Williamson, I. A. D., Minkov, M. & Fan, S. Wave physics as an analog recurrent neural network. *Sci. Adv.* **5**, eaay6946 (2019).

29. Mohammadi Estakhri, N., Edwards, B. & Engheta, N. Inverse-designed metastructures that solve equations. *Science* **363**, 1333–1338 (2019).

30. Camacho, M., Edwards, B. & Engheta, N. A single inverse-designed photonic structure that performs parallel computing. *Nat. Commun.* **12**, 1466 (2021).

31. Arfken, G. B., Weber, H. J. & Harris, F. E. *Mathematical Methods for Physicists* (Elsevier, 2013).

32. Oldenburger, R. Infinite powers of matrices and characteristic roots. *Duke Math. J.* **6**, 357–361 (1940).

33. Molesky, S. et al. Inverse design in nanophotonics. *Nat. Photon.* **12**, 659–670 (2018).

34. Piggott, A. Y. et al. Inverse design and demonstration of a compact and broadband on-chip wavelength demultiplexer. *Nat. Photon.* **9**, 374–377 (2015).

35. Sell, D., Yang, J., Doshay, S., Yang, R. & Fan, J. A. Large-angle, multifunctional metagratings based on freeform multimode geometries. *Nano Lett.* **17**, 3752–3757 (2017).

36. Lalau-Keraly, C. M., Bhargava, S., Miller, O. D. & Yablonovitch, E. Adjoint shape optimization applied to electromagnetic design. *Opt. Express* **21**, 21693 (2013).

37. Hughes, T. W., Minkov, M., Williamson, I. A. D. & Fan, S. Adjoint method and inverse design for nonlinear nanophotonic devices. *ACS Photon.* **5**, 4781–4787 (2018).

38. Green, M. A. Self-consistent optical parameters of intrinsic silicon at 300 K including temperature coefficients. *Sol. Energy Mater. Sol. Cells* **92**, 1305–1310 (2008).

39. Kelly, R. L. Program of the 1972 Annual Meeting of the Optical Society of America. *J. Opt. Soc. Am.* **62**, 1336 (1972).

40. Malitson, I. H. Interspecimen comparison of the refractive index of fused silica. *J. Opt. Soc. Am.* **55**, 1205–1209 (1965).

41. Jiang, J. et al. Free-form diffractive metagrating design based on generative adversarial networks. *ACS Nano* **13**, 8872–8878 (2019).

42. Goodman, J. W., Dias, A. R. & Woody, L. M. Fully parallel, high-speed incoherent optical method for performing discrete Fourier transforms. *Opt. Lett.* **2**, 1–3 (1978).

43. Athale, R. A. & Collins, W. C. Optical matrix–matrix multiplier based on outer product decomposition. *Appl. Opt.* **21**, 2089–2090 (1982).

44. Farhat, N. H., Psaltis, D., Prata, A. & Paek, E. Optical implementation of the Hopfield model. *Appl. Opt.* **24**, 1469–1475 (1985).

45. Zhu, W., Zhang, L., Lu, Y., Zhou, P. & Yang, L. Design and experimental verification for optical module of optical vector–matrix multiplier. *Appl. Opt.* **52**, 4412–4418 (2013).

46. Spall, J., Guo, X., Barrett, T. D. & Lvovsky, A. I. Fully reconfigurable coherent optical vector–matrix multiplication. *Opt. Lett.* **45**, 5752–5755 (2020).

47. Rosenblatt, G., Simkhovich, B., Bartal, G. & Orenstein, M. Nonmodal plasmonics: controlling the forced optical response of nanostructures. *Phys. Rev. X* **10**, 011071 (2020).

48. Li, L. Bremmer series, R-matrix propagation algorithm, and numerical modeling of diffraction gratings. *J. Opt. Soc. Am. A* **11**, 2829–2836 (1994).

49. Sukham, J., Takayama, O., Lavrinenko, A. V. & Malureanu, R. High-quality ultrathin gold layers with an APTMS adhesion for optimal performance of surface plasmon polariton-based devices. *ACS Appl. Mater. Interfaces* **9**, 25049–25056 (2017).

50. Verschuuren, M. A., Knight, M. W., Megens, M. & Polman, A. Nanoscale spatial limitations of large-area substrate conformal imprint lithography. *Nanotechnology* **30**, 345301 (2019).

51. Lalanne, P., Hugonin, J. P. & Chavel, P. Optical properties of deep lamellar gratings: a coupled Bloch-mode insight. *J. Light. Technol.* **24**, 2442–2449 (2006).

Methods

Fabrication

The sample was fabricated following the steps below:

- The c-Si on Al_2O_3 substrates were acquired from MTI. The c-Si (orientation, (100)) layer was 500 nm thick, polished (surface roughness, <2.5 nm) and undoped. The sapphire (orientation, R-plane) substrate was 0.46 mm thick and double-side polished (surface roughness, <0.3 nm on the front side and optical grade polish on the back). The substrate was cleaned in base piranha, and the c-Si was etched to the final metasurface thickness ($h = 150$ nm) via reactive ion etching employing CHF_3, SF_6 and O_2. The c-Si film thickness was checked with Filmetrics F20.
- After an O_2 plasma surface treatment, a 50-nm-thick layer of hydrogen silsesquioxane negative-tone resist was spin-coated and baked for 2 min at 180 °C.
- The metasurface was patterned into the hydrogen silsesquioxane layer by exposure using a Raith Voyager electron-beam lithography system (50 kV, dose 2,300 μC cm^{-2}) and development in tetramethylammonium hydroxide for 60 s at 50 °C.
- The pattern was then transferred into the c-Si by a two-step reactive ion etching process employing Cl_2, HBr and O_2. Next, the sample was cleaned in acid piranha for 10 minutes.
- After another O_2 plasma surface treatment, a 100-nm-thick layer of SiO_2 sol–gel (Nanoglass E1200 3:1 in 1-butanol)[50] was spin-coated and baked for 3 min at 45 °C and 2 min at 200 °C. This step was repeated three times.
- The sample was annealed at 800 °C for 10 min. The temperature was ramped up from room temperature to 800 °C in 8 min and, after 10 min, ramped down again to room temperature in 5 min.
- The SiO_2 thickness was checked with Filmetrics F20 and a profilometer (KLA, Tencor P7). Additional SiO_2 was sputtered with Polyteknik Flextura M506 S using a Si source until a total thickness of 638 nm was reached.
- A 3-aminopropyl trimethoxysilane adhesion monolayer was chemically deposited on the sample[49].
- A 15-nm-thick Au layer was evaporated with a Polyteknik Flextura M508 E electron-beam evaporator.

Optical characterization

The data in Fig. 4c,e were collected with a Spectra Pro 2300i spectrometer equipped with a Pixis 400 CCD (charge-coupled device). The sample was illuminated with collimated white light from a SuperK EXTREME/FIANIUM supercontinuum laser. The zeroth-order transmitted light was collected by an integrating sphere and sent to the spectrometer through a multimode fibre. Light was polarized as depicted in Fig. 2a (TE).

The data in Fig. 5 were collected with a different configuration. The illumination was provided by the same SuperK EXTREME/FIANIUM supercontinuum white light laser that was monochromated (2 nm bandwidth) by a Laser Line Tunable Filter from Photon Etc. The set-up consisted of two concentric rotating stages. The sample was mounted on the inner rotating stage (Rot. stage 1 in Supplementary Fig. 8) while an optical power meter (PM100USB with photodiode power sensor S121C from Thorlabs) was mounted on the outer rotating stage (Rot. stage 2). This configuration allows independent control of the input (θ_0) and output (θ_t) angles. Light is polarized before impinging on the sample, and the illumination and collection angles are changed as the wavelength is swept following the grating equation.

Data availability

The data that support the findings of this study are available from the corresponding author upon reasonable request.

Code availability

All codes produced during this research are available from the corresponding author upon reasonable request.

Author contributions

A.C. designed and fabricated the samples, performed the numerical simulations and performed the optical measurements. A.C., B.E. and V.N. performed the theoretical analyses. A.A., N.E. and A.P. supervised the project. All authors contributed to the analysis and writing of the paper.

Competing interests

The authors declare no competing interests.

Additional information

Supplementary information The online version contains supplementary material available at https://doi.org/10.1038/s41565-022-01297-9.

Correspondence and requests for materials should be addressed to Andrea Cordaro.

Peer review information *Nature Nanotechnology* thanks Arkaprovo Das, Xiaowen Dong and the other, anonymous, reviewer(s) for their contribution to the peer review of this work.

Reprints and permissions information is available at www.nature.com/reprints.